


On the unsteadiness of shock–laminar boundary layer interactions of hypersonic flows over a double cone

Cite as: Phys. Fluids **30**, 106111 (2018); <https://doi.org/10.1063/1.5047791>

Submitted: 09 July 2018 . Accepted: 25 September 2018 . Published Online: 31 October 2018

Ozgur Tumuklu , Vassilis Theofilis, and Deborah A. Levin

COLLECTIONS

 This paper was selected as Featured



View Online



Export Citation



CrossMark

ARTICLES YOU MAY BE INTERESTED IN

[Investigation of unsteady, hypersonic, laminar separated flows over a double cone geometry using a kinetic approach](#)

Physics of Fluids **30**, 046103 (2018); <https://doi.org/10.1063/1.5022598>

[Aerodynamic heating in transitional hypersonic boundary layers: Role of second-mode instability](#)

Physics of Fluids **30**, 011701 (2018); <https://doi.org/10.1063/1.5005529>

[Oscillation of the shock train in an isolator with incident shocks](#)

Physics of Fluids **30**, 116102 (2018); <https://doi.org/10.1063/1.5053451>

Scilight Highlights of the best new research
in the physical sciences

[LEARN MORE!](#)



On the unsteadiness of shock–laminar boundary layer interactions of hypersonic flows over a double cone

Ozgur Tumuklu,^{1,a)} Vassilis Theofilis,^{2,b)} and Deborah A. Levin^{1,c)}

¹Department of Aerospace Engineering, University of Illinois at Urbana-Champaign, Urbana, Illinois 61801, USA

²School of Engineering, University of Liverpool, Liverpool L69 3GH, United Kingdom

(Received 9 July 2018; accepted 25 September 2018; published online 31 October 2018)

Unsteadiness of axisymmetric shock-dominated hypersonic laminar separated flow over a double cone is studied for the first time using a combination of time accurate Direct Simulation Monte Carlo (DSMC) calculations, linear global instability analysis, and momentum potential theory (MPT). Close to steady state linear analysis reveals the spatial structure of the underlying temporally stable global modes. At all Reynolds numbers examined, the amplitude functions demonstrate the strong coupling between the separated flow region at the cone junction with the entire shock system, including pressure and temperature waves generated behind the shock and spatially amplified Kelvin-Helmholtz waves. In addition, as the Reynolds number is increased, temporally damped harmonic shock oscillations and multiple-reflected λ -shock patterns emerge in the eigenfunctions. Application of the MPT (valid for both linear and nonlinear signals) to the highest Reynolds number DSMC results shows that large acoustic and thermal potential variations exist in the vicinity of the separation shock, the λ -shock patterns, and the shear layers. It is further shown that the motion of the bow shock system is highly affected by non-uniformities in the acoustic field. At the highest Reynolds number considered here, the unsteadiness is characterized by Strouhal numbers in the shear layer and bow-shock regions and is found to be in qualitative agreement with earlier experimental and numerical work. *Published by AIP Publishing.* <https://doi.org/10.1063/1.5047791>

I. INTRODUCTION

Laminar-turbulent transition in hypersonic, shock-wave laminar boundary layer interactions (SLBLIs) is characterized by spatial regions featuring both sub- and supersonic flows, multiple length scales, and regions with distinct degrees of thermochemical non-equilibrium. Aspects of linear instability of hypersonic shock-dominated flows have been addressed by a number of authors over the years.^{1–3} In hypersonic flows over a double cone geometry, the existence of an underexpanded jet in the shock-laminar separation bubble interaction region is characterized as an Edney type IV pattern⁴ that exhibits inherent instabilities due to the high-frequency unsteady movement of the jet.⁵ Despite the studies of Duck *et al.*⁶ and Cassel *et al.*,⁷ the present-day understanding of the time evolution of SLBLI instabilities in the supersonic regime remains incomplete and, as a consequence, predictions of all-important surface properties such as heat flux remain far from satisfactory. An additional stumbling block for analyzing instabilities of hypersonic flows is the lack of an accurate description of the non-continuum effects of velocity and temperature slip at the leading edge and their relation to the observed flow unsteadiness.

Laminar and turbulent shock-induced separated flows are susceptible to unsteadiness that can be characterized by a wide range of frequencies depending on the upstream or

downstream forcing mechanism.^{4,8} In particular, for the incipient-separation class, the mean flow has no reverse velocity and the high-frequency motion of the separation shock for a turbulent boundary layer is directly related to upstream influences primarily due to the incoming turbulence, resulting in higher frequencies of the shock unsteadiness. On the other hand, for strongly and moderately separated flows, low frequency (i.e., approximately two orders of magnitude lower than the incoming turbulence), large-scale motions in the intermittent region are under the influence of both upstream and downstream flow characteristics. Narayanaswamy *et al.*⁹ showed that the upstream flow characteristics have a significant impact on the shock dynamics based on the experiments of a pulsed-plasma jet actuator, aiming to control the unsteadiness of the shock motions. Moreover, Priebe and Martin¹⁰ showed that relatively lower correlations were observed between fluctuations in the mass flux in the upstream boundary layer and the separation shock in comparison to the downstream mechanism. In order to investigate the main parameters having an influence on the time scale of low-frequency shock motion more closely, Piponniau *et al.*¹¹ conducted a theoretical study to determine the driving mechanism of the low-frequency shock motion and found that these low-frequency shock oscillations can be attributed to the unbalanced mass flux of the separation zone for moderately low Mach number flows over relatively simple geometries.

In our previous work,¹² we presented the first time accurate DSMC simulations of shock-dominated hypersonic laminar flows over a double cone for increasing Reynolds numbers at a Mach number of about 16. The main flow features, such as

^{a)}tumuklu2@illinois.edu

^{b)}Also at: Universidade Federal Fluminense, Niteroi, Rio de Janeiro, Brazil.
Electronic mail: v.theofilis@liverpool.ac.uk

^{c)}deblevin@illinois.edu

the strong bow-shock, the location of the separation shock, the triple point, and the entire laminar separated region, showed a time-dependent behavior, and, although the separation shock angle was found to be similar for all Re numbers, the effects of Reynolds numbers on the structure and extent of the separation region were found to be profound. The paper established that with the correct selection of numerical parameters and ensemble sampling techniques, DSMC could successfully be used to model these unsteady, near-continuum flows. The DSMC simulations enabled us to study the importance of thermal nonequilibrium on the relative magnitude of the ratio of specific heats which plays a critical role in SWBLIs. Also, only possible with a kinetic method, velocity distribution functions were obtained at different locations in the flow and showed the classic bi-modal distribution behavior in the bow shock, but were nearly Maxwellian at locations near the leading edge and separation points. The study of surface parameters such as velocity and temperature-slip, heat flux, and coefficient of friction showed a number of important results. To characterize the unsteady behavior of the double cone flow and its change with Reynolds numbers, the residual algorithm was applied to the unsteady DSMC signal to obtain the average damping rate and amplitude function that corresponds to the least damped eigenmode. It was found that for all Reynolds numbers except the highest case, the time evolution of all flow quantities such as velocities, temperatures, and pressures could be fit by a single eigenmode; however, this became more difficult for the highest Reynolds number case.

The nature of the disturbances and how they might change as a function of Reynolds numbers, however, was not addressed. Furthermore, although the DSMC time traces of pressure and translational temperature showed low frequency oscillations in the boundary layer somewhat similar to those in the bow shock, no attempt was made to connect them to previous measurements and simulations. The objective of the present work is to combine for the first time Direct Simulation Monte Carlo (DSMC) methods with linear global stability analysis and momentum potential theory¹³ to analyze mechanisms that cause the unsteadiness in SLBLI on the well-known sharp 25°/55° double cone model¹⁴ at Mach numbers $Ma \approx 16$, Knudsen numbers $4 \times 10^{-4} \leq Kn \leq 2 \times 10^{-3}$, and unit Reynolds numbers $9.35 \times 10^4 \leq Re \leq 3.74 \times 10^5 \text{ m}^{-1}$. Here, a link is established between flow unsteadiness and its linear global (in)stability. First, the residuals algorithm of Theofilis¹⁵ is employed to extract from time-accurate DSMC simulation data the amplitude functions of the global eigenmode, describe the features of its spatial structure, and monitor the changes that it undergoes as flow parameters change. It is shown that, as the Reynolds number is increased, the degree and nature of unsteadiness of SLBLI over the double cone undergo qualitative and quantitative changes. Subsequently, flow unsteadiness, attributed by McKenzie and Westphal¹⁶ to interactions of acoustic and thermal disturbance waves with shock waves and the hypersonic boundary layer, is re-examined without the simplifying assumptions of the earlier analyses.¹⁶ To this end, MPT is employed to decompose the unsteady DSMC flow field into its hydrodynamic (vortical), acoustic, and thermal components and understand the underlying mechanisms responsible for the observed changes in the

amplitude functions of the global eigenmodes, as well as to identify and classify inter-modal energy transfer phenomena and sound generation mechanisms. Unlike the classic Kovaszny¹⁷ decomposition, in which modes can only be decoupled when the amplitude of these disturbances is small, MPT does not require one to invoke an assumption of linearity of the perturbations, as has been recently discussed by Unnikrishnan and Gaitonde.¹⁸ In Sec. II, the main features of the base state are summarized. Section III discusses the theoretical background of the residuals algorithm and MPT. Section IV presents the amplitude functions of the global modes at this Mach number, the effect of changes that the modes undergo as the Reynolds number increases, and a discussion of the effect of hydrodynamic, acoustic, and entropy perturbations on the global eigenvectors. A short discussion summarizes the present results.

II. BASE FLOW FEATURES

The base flow has been simulated using DSMC, a stochastic approach to solving the Boltzmann equation.¹⁹ DSMC is well suited for capturing the transient behavior of viscous laminar unsteady hypersonic flows toward transition at moderate and high Knudsen numbers because it is time-accurate, provides the highest fidelity of molecular thermal nonequilibrium treatment, and inherently captures velocity and temperature slip without the need to assume *a priori* specific models. The free stream conditions for the simulations taken from Holden *et al.*¹⁴ are a vibrational temperature of 1986 K, translational and rotational temperatures equilibrated at 42.6 K, a Mach number of 15.8, a pressure of 2.2 Pa, and a stagnation enthalpy of 2.2 MJ/kg. This case corresponds to a unit Reynolds number of $Re = 9.35 \times 10^4 \text{ m}^{-1}$ and is denoted as the *low- Re case* in what follows. To increase the Reynolds numbers, these conditions are kept constant, but the freestream static pressure is gradually increased from the *low- Re case* of 2.2 to 4.4 and 8.8 Pa for the *moderate-* and *high- Re cases*, respectively. It should be noted that all length scales, velocities, and times are normalized with respect to the length of the first cone, $L = 0.1016 \text{ m}$, a freestream velocity of $U_\infty = 2073 \text{ m s}^{-1}$, and the characteristic time required for the undisturbed flow to travel along the first cone, L/U_∞ , respectively. Similarly, a total temperature of 1907 K and a maximum pressure of 1425 Pa of the *low- Re case* are used to normalize the temperature and pressure values.

The shock wave flow pattern that develops in the high- Re simulation is seen in the computed Schlieren contours of the density gradient shown in Fig. 1. The oblique shock emanating from the leading edge of the first cone interacts with the detached bow shock formed at the second cone. These outer shocks are further modified by an extensive and strong separation zone with the associated separation (S) and reattachment (R) points, the triple point (T), and a contact surface passing through point M. The result is a flow field with complex features such as shock impingement, shear layers, and boundary layer interactions. The supersonic flow in the region bounded by points T, M, and R is compressed by a high-pressure subsonic flow due to the strong bow shock, resulting in an underexpanded flow confined by two contact surfaces:

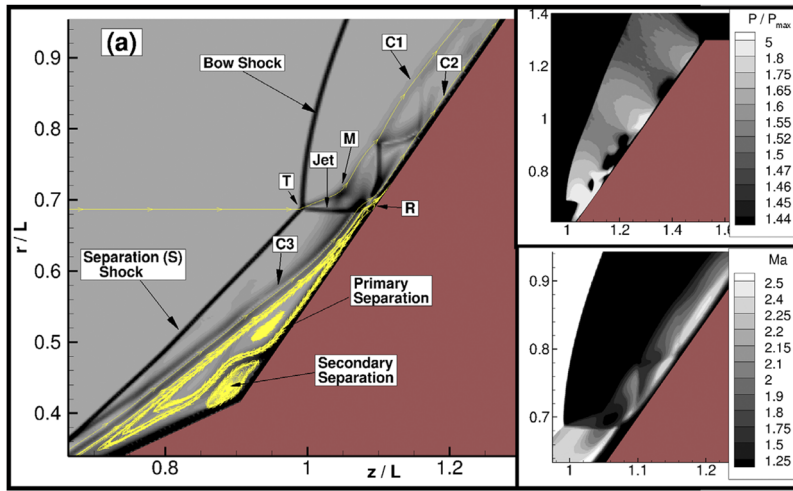


FIG. 1. Computed Schlieren image of the high $-Re$ case at $t = 30.6$; T: triple point; R: reattachment shock; C1, C2, and C3: contact discontinuity surfaces. The insets are the normalized pressure P/P_{max} and Mach contours in the neighborhood of the triple point, and the yellow lines show the streamlines.

C1 is formed between the subsonic hot stream and the cold supersonic jet, whereas C2 is formed between the boundary layer and the supersonic cold jet.⁵ The underexpanded flow passes between C1 and C2 with a series of compressible and expanded waves to direct the jet through the cone surface, creating pressure variations along the second cone surface as can be seen in the inset of Fig. 1.

Turning to gas-surface properties, Fig. 2 shows the Reynolds number variation of skin friction and velocity slip. As shown in Fig. 2(a), it was found that the skin friction coefficient along the first cone surface decreases with the square root of the Reynolds number, which is consistent with classic boundary layer theory. By contrast, the high $-Re$ case exhibits a larger separation region and shows stronger fluctuations in the aft part of the cone. The normalized velocity slip shown in Fig. 2(b) at the leading edge is highest due to a larger local Kn, reaching values of up to 0.097, and although decreasing in magnitude with decreasing Kn numbers was still relatively large at the leading edge of the first cone. Predictions of heat flux for the lowest Reynolds number case compare well with the experiment of Holden *et al.*¹⁴ especially in the separation region indicated by decreasing heat flux values. The two DSMC simulations differing by a factor of four in the number of particles and collision cells and two in the time step

strongly demonstrate the convergence of DSMC numerical parameters.^{12,20}

III. THEORETICAL BACKGROUND

A. The residuals algorithm

The algorithm¹⁵ was originally proposed to relate the time-accurate signal in direct numerical simulations of incompressible lid-driven cavity flow with the least-damped global eigenmodes of this flow and has since been used to compute damped global modes in a number of configurations.^{21,22} A brief description, as applicable to zero-frequency perturbations, follows. Near convergence of the DSMC simulations to a steady state, the least-damped eigenmode properties, such as the damping rate, frequency, and spatial structure of the amplitude functions, can be recovered by post-processing of the time-accurate signals of all macroscopic flow quantities computed in the simulations, $\mathbf{q} = (u, v, T_{tm}, T_{rot}, T_{vib}, P)^T$, where the six variables denote axial and radial velocity components, translational, rotational, and vibrational temperatures, and pressure, respectively. Linear stability theory assumes that the full flowfield, $\mathbf{q}(x, y, t)$, is a linear superposition of the steady solution, $\bar{\mathbf{q}}(x, y)$, toward which the time-accurate

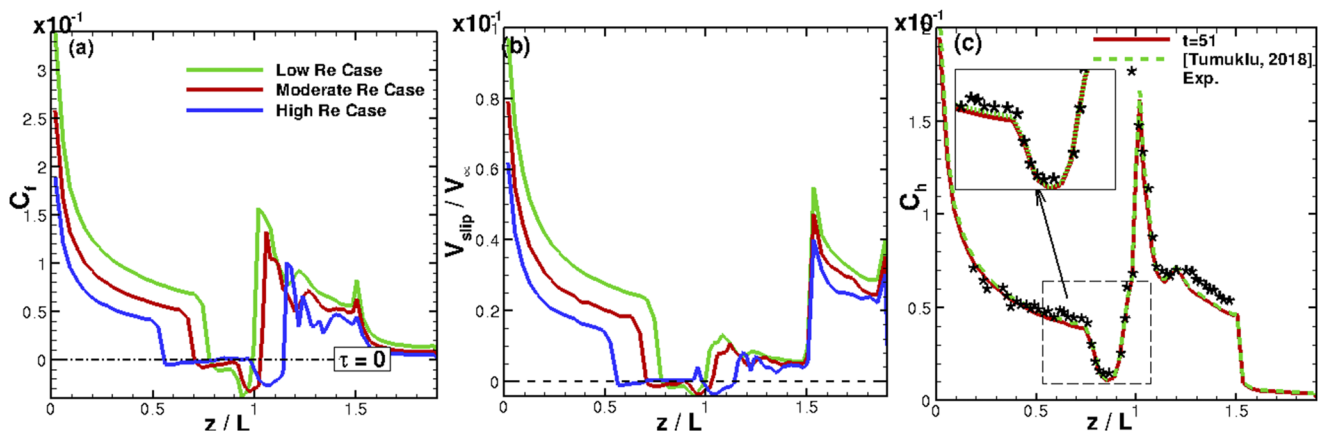


FIG. 2. Effects of the Reynolds number on surface parameters: (a) skin friction coefficient, (b) normalized velocity slip, and (c) heat flux coefficient for the low Re case.

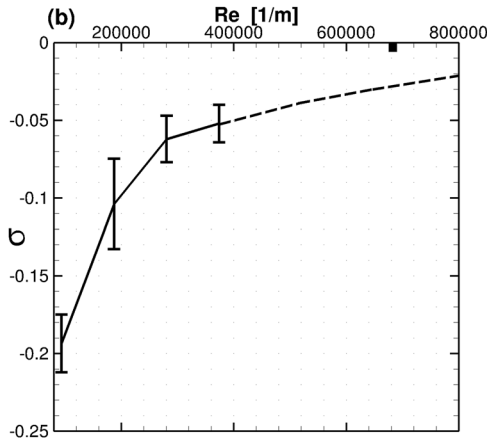


FIG. 3. Variation of the decay rate of the least damped eigenfunction with Re numbers. The black square represents an unsteady flow of $M = 11.27$ for the hollow flare configuration with 45° taken from Ref. 23.

simulation is marched, and a small-amplitude unsteady *residual* deviation from this steady state, $\tilde{\mathbf{q}}(x, y, t)$, with $\epsilon \ll 1$ [i.e., $\mathbf{q}(x, y, t) = \bar{\mathbf{q}}(x, y) + \epsilon \tilde{\mathbf{q}}(x, y, t)$]. In order to verify the applicability of linear stability theory, probes were placed in the flowfield to monitor the DSMC signal, until the residuals were sufficiently small for linear theory to apply and the monotonic exponential decay of the residual amplitude to be observed in time. The damping rate, σ , shown in Fig. 3, was found to be real and was calculated from the logarithmic time-derivative of the DSMC signal¹² at two times t_1 and t_2 , at which the following 2×2 system can be written:

$$\mathbf{q}(x, y, t_1) = \bar{\mathbf{q}}(x, y) + \epsilon \hat{\mathbf{q}}_r e^{\sigma t_1}, \quad (1)$$

$$\mathbf{q}(x, y, t_2) = \bar{\mathbf{q}}(x, y) + \epsilon \hat{\mathbf{q}}_r e^{\sigma t_2}. \quad (2)$$

This system can be solved to predict the unknown amplitude functions $\hat{\mathbf{q}}_r(x, y)$ and also the base state $\bar{\mathbf{q}}(x, y)$ toward which the DSMC is converging well before the simulation reaches convergence.

The role of statistical noise in DSMC has been examined since it may affect the quality of the simulations and, in turn, the accuracy of the predictions of the residuals algorithm. Predictions of the residuals algorithm for the base flow, presented in detail by Tumuklu *et al.*,¹² are, respectively, within 0.05% and 5% of the asymptotic time-dependent DSMC solution for the low and high Reynolds number cases, which implicitly suggests that the damping rate estimation is within the same confidence level. Interestingly, the times t_1 and t_2 are taken approximately in the middle of the length of time needed for the DSMC to converge to a time-independent state, which implies large savings in the cost of the computation. Computed damping rates were found to be invariant to the locations at which probes were placed in the flowfield, or to the choice of the times at which the signal was analyzed, provided that the corresponding residuals are small in amplitude. However, for the highest Reynolds number simulations, discrepancies were observed along the contact surface, C1. This is not due to inadequate DSMC numerical parameters but rather suggests that the predicted eigenmode undergoes a qualitative change compared with the lower Reynolds number simulations. In fact, increasing the Reynolds number by a factor of two in comparison to

the moderate $-Re$ case results in a Kelvin-Helmholtz (KH) instability along the edge of the second cone, arising at the shear layer, and the flow does not reach the steady state, even though the simulation was run three times further in time as compared to the moderate $-Re$ case, as will be discussed further in Sec. IV.

B. Momentum potential theory

The physical mechanisms that drive unsteadiness in the flow at the highest Reynolds number case have been analyzed using Momentum Potential Theory (MPT)¹³ to identify thermal and acoustic modes in the DSMC results. In MPT, the momentum density term can be written as

$$\rho \mathbf{u} = \mathbf{B} - \nabla \phi, \quad (3)$$

where the linear momentum density, $\rho \mathbf{u}$, can be decomposed into solenoidal (i.e., $\nabla \cdot \mathbf{B} = 0$) and irrotational ($\nabla \phi$) components based on a Helmholtz decomposition. The solenoidal component, also known as the hydrodynamic mode, can further be split into its mean ($\bar{\mathbf{B}} = \overline{\rho \mathbf{u}}$) and unsteady portion (\mathbf{B}'), whereas the scalar potential (ϕ) can be divided into acoustic (ϕ_A) and thermal (ϕ_T) parts,

$$\phi = \phi_A + \phi_T. \quad (4)$$

Taking the divergence of both sides of Eq. (3) and using mass conservation, Eq. (3) can be written as

$$\frac{\partial \rho}{\partial t} = \nabla^2 \phi. \quad (5)$$

The constitutive relation for a single species flow can be written in the form of¹³

$$\rho = \rho(p, S), \quad (6)$$

where p is the pressure and S is the entropy. Since the density is a thermodynamic state variable, its time dependence can be associated with acoustic and thermal parts.¹³ That is,

$$\frac{\partial \rho}{\partial t} = \frac{1}{c^2} \frac{\partial p}{\partial t} + \frac{\partial \rho}{\partial S} \frac{\partial S}{\partial t}, \quad (7)$$

where the first term on the RHS corresponds to the acoustic field and may be related to the acoustic portion of the potential as

$$\frac{1}{c^2} \frac{\partial p}{\partial t} = \nabla^2 \phi_A \quad (8)$$

and c is the speed of sound calculated based on the local temperature and specific heat ratio (γ), and the second term on the RHS is associated with the thermal part of the scalar potential, as discussed by Doak.¹³

In Ref. 12, it was shown that the exponentially decaying mode is the leading perturbation throughout the domain, coupling in the separation, bow shock, and shear layer regions together through the global mode amplitude function, as will be seen shortly in Sec. IV. Consequently, Eqs. (1) and (2) can be substituted into Eq. (5) to obtain

$$\nabla^2 \phi = \hat{\rho} \sigma e^{\sigma t}, \quad \nabla^2 \phi_A = \frac{1}{c^2} \hat{p} \sigma e^{\sigma t}, \quad (9)$$

where $\hat{\rho}$ and \hat{p} are the density and pressure amplitude functions of the least damped eigenmode. Therefore, the amplitude functions calculated based on the time-accurate DSMC data can be used to determine the scalar potentials.

In the work of Unnikrishnan and Gaitonde,¹⁸ Doak's momentum potential theory was applied to a large-eddy simulation of a turbulent jet expansion to analyze the contribution of acoustic, hydrodynamic, and thermal disturbance modes to the perturbation energy. Equation (3) was expanded as

$$\overline{\rho\mathbf{u}} + (\rho\mathbf{u})' = \overline{\mathbf{B}} + \mathbf{B}' - \nabla\overline{\phi} - \nabla\phi', \quad (10)$$

where the bar and primed symbols represent mean and fluctuating (time-dependent) components and the flow was assumed to be time-stationary, i.e.,

$$(1/2T) \int_{-T}^T \rho'(x, t) dt = 0. \quad (11)$$

Since the mean solenoidal component, $\overline{\mathbf{B}}$, is equal to the mean potential density term, $\overline{\rho\mathbf{u}}$, the fluctuating momentum density term becomes

$$(\rho\mathbf{u})' = \mathbf{B}' - \nabla\phi'. \quad (12)$$

It should also be noted that Eqs. (3) and (12) are of the same form except that the overall flowfield (mean + fluctuating terms) is replaced with the corresponding fluctuating term. In our case, however, the flow is not time stationary and Eq. (3) must be used.

To solve Eq. (9) using the DSMC solution, proper boundary conditions must be defined. Since the momentum density at the domain outer boundaries and the cone surface have reached the steady state, consistent with the application of the residuals algorithm method, it can be assumed that the irrotational component of the momentum density at the boundaries is zero and a Neumann boundary condition was used along the $r = 0$ line since the cone configuration is axisymmetric, as shown in Fig. 4. Similar to the work of Ref. 18, a ‘‘sponge zone boundary’’ was implemented to dampen outer disturbances. The solution of Poisson's equation was performed on a Cartesian mesh twice as coarse as the size of the DSMC collision cell with a constant spatial resolution of 401 intervals in the axial and radial directions. Note, however, that the DSMC collision cell size, which is smaller than the local mean free path, is about a factor of 80 smaller than the Poisson solver mesh size. For the highest Re number case where there are large density gradients in the flowfield, the Poisson mesh resolution was increased by a factor of two to test the sensitivity of the

solution to Eqs. (4) and (8). The largest percentage difference in the gradients of the acoustic and thermal fields was found to be $\sim 30\%$ and occurred only at the outer boundaries of the domain.

IV. RESULTS

A. Predictions of linear stability analysis

Steady laminar flows were obtained in the Reynolds number range examined in this work. Close to convergence to a steady state, curve-fits of the DSMC signal were performed in order to extract the (non-dimensional) damping rates, σ . The result is shown in Fig. 3 for the low, moderate, and high- Re numbers plus one additional case corresponding to a pressure of 6.6 Pa. As expected, the damping rate of the least damped global eigenmode is seen to decrease systematically, as the Reynolds number increases. The effect of the curve-fit parameters on the estimation of σ was monitored, and the variation of σ at each Reynolds number is shown as an error bar in Fig. 3. This variation was found to be associated with the choice of different macroscopic flow variables at different locations in the field, while the use of a relatively large number of DSMC particles in a background cell ensured that the flow was adequately resolved and did not affect the damping rate estimation or the applicability of the residuals algorithm. Once the decay rates were estimated at randomly chosen times during the exponential decay of the DSMC signal, the 2×2 system (1-2) was solved to compute the amplitude functions of the components of the least damped global mode eigenvector, $\hat{\mathbf{q}}_r(x, y) = (\hat{u}, \hat{v}, \hat{T}_{tm}, \hat{T}_{rot}, \hat{T}_{vib}, \hat{P})^T$. The amplitude functions have been computed at all Reynolds numbers studied and normalized with the corresponding aforementioned scales. Results for the three Reynolds numbers are shown in Figs. 5–7. We emphasize that using values of σ within the error bars shown in Fig. 3 does not alter the spatial structure of the amplitude functions shown.

The most noteworthy feature of the least damped global mode is that, at all Reynolds numbers examined, the spatial distributions of the amplitude functions of its components closely follow both the strong shock and the outline of the laminar separation region of the underlying steady laminar base flow. Based on the comparable magnitude of the amplitude functions and the common damping rate at the separation and bow shock locations, it can be asserted that the entire primary shock and the laminar separation region at the cone junction are strongly coupled with each other, emphasizing that any changes in any part of either of these will influence the other in a manner similar to that discussed in the earlier work of Ref. 24.

Specific features observed in the low Reynolds number amplitude functions concern the axial component, \hat{u} , of the perturbation velocity, which is found to decrease inside the shock as well as in the separation region, as seen in Fig. 5(a). The opposite behavior is observed for the radial component of the velocity perturbation, \hat{v} , as seen in Fig. 5(b). The effect of thermal nonequilibrium on the amplitude functions is also distinctive for the three temperature perturbation components. The amplitude function of the translational and rotational temperature perturbations, \hat{T}_{tm} and \hat{T}_{rot} , seen in Figs. 5(c) and 5(d) is found to have an analogous spatial structure as the

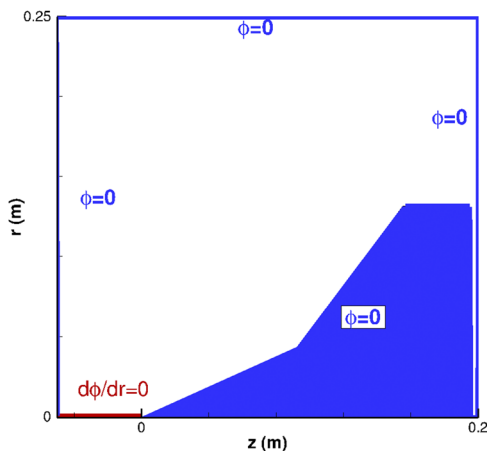


FIG. 4. Domain and boundary conditions for the Poisson solver.

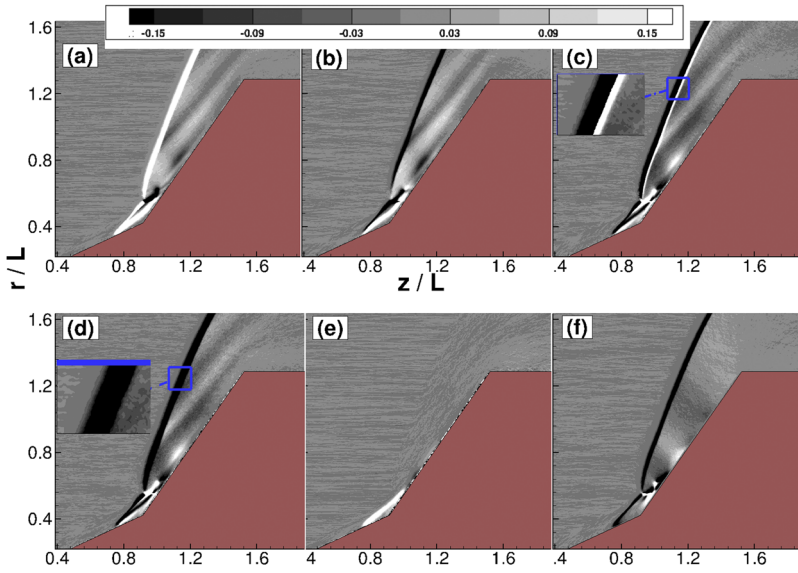


FIG. 5. Normalised amplitude functions of least-damped linear global mode at $Re = 93\,500\text{ m}^{-1}$. (a) x-velocity field, \hat{u} ; (b) y-velocity field, \hat{v} ; (c) translational temperature, \hat{T}_{trn} ; (d) rotational temperature, \hat{T}_{rot} ; (e) vibrational temperature, \hat{T}_{vib} ; (f) pressure, \hat{P} .

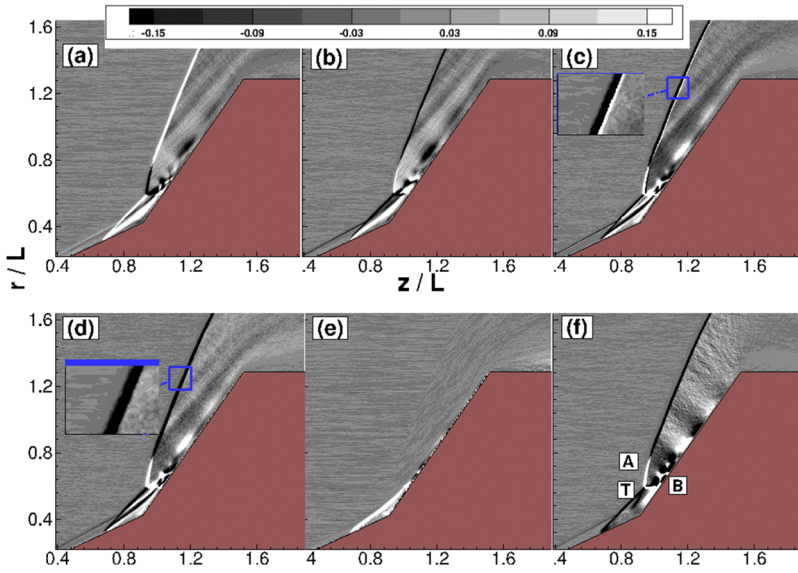


FIG. 6. Normalised amplitude functions of least-damped linear global mode at $Re = 187\,000\text{ m}^{-1}$. (a) \hat{u} ; (b) \hat{v} ; (c) \hat{T}_{trn} ; (d) \hat{T}_{rot} ; (e), \hat{T}_{vib} ; (f) \hat{P} .

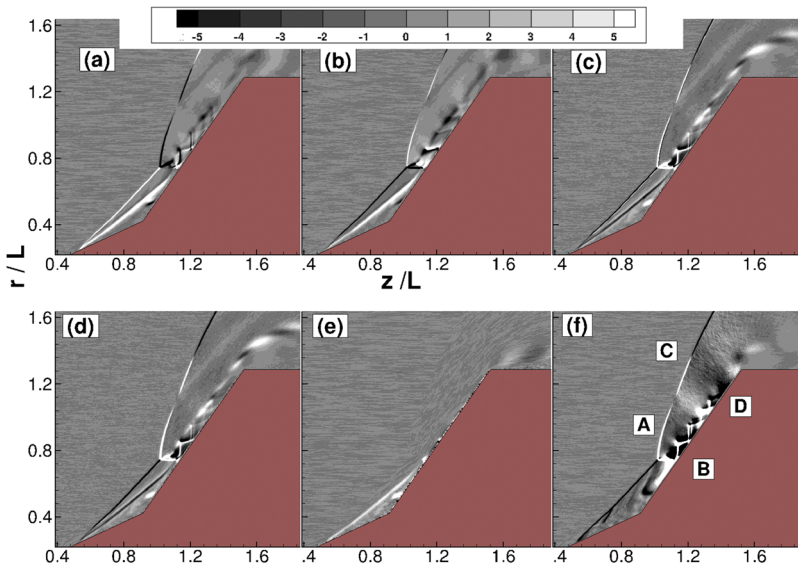


FIG. 7. Normalised amplitude functions of least-damped linear global mode at $Re = 374\,000\text{ m}^{-1}$. (a) \hat{u} ; (b) \hat{v} ; (c) \hat{T}_{trn} ; (d) \hat{T}_{rot} ; (e), \hat{T}_{vib} ; (f) \hat{P} .

velocity perturbations, which may be explained by the high relaxation rate of these two modes. The sign change of the translational temperature downstream of the bow shock occurs because the translational energy decreases suddenly due to thermal relaxation with the internal modes. By contrast, the amplitude function of the vibrational temperature, \hat{T}_{vib} , seen in Fig. 5(e), is practically confined in its entirety within the separation region. Finally, the spatial distribution of the pressure perturbation, \hat{P} , seen in Fig. 5(f), clearly shows the same coupling between the primary shock system and the separation zone, as well as streamwise periodic pressure perturbations on the downstream cone surface.

As the Reynolds number is increased, the above described features of the least damped global eigenmode undergo qualitative changes in different regions of the domain, as shown in Figs. 6 and 7. In Fig. 6, a sign change in the amplitude function and the incipient presence of λ -shocklets may be observed. As has been shown by Duck *et al.*,⁶ the interactions of self-induced acoustic and thermal disturbance waves with shock waves and the hypersonic boundary layer can cause flow unsteadiness.⁶ For the high Re number case, note that a different grayscale is used to show the increased strength of the perturbations. Shock oscillations appear on the bow shock, while the amplitude functions \hat{u} , \hat{v} , \hat{T}_{tm} , \hat{T}_{tot} , and \hat{P} also connect at the triple point shock perturbations with those in the (now substantially larger) separation zone. By contrast, \hat{T}_{vib} is again confined within the separation region, although at this Reynolds number this amplitude function features additional peaks at the downstream cone wall; the latter could be interpreted as boundary layer perturbations, although the resolution of the boundary layer at this Reynolds number is extremely challenging.

However, perhaps the most striking common feature of the high- Re amplitude functions is the repeating diagonal λ -shocklet structures between the two sonic lines, seen as a base flow feature in Fig. 1. These structures, further discussed in Sec. IV B, are attributed to the existence of expansion and compression waves, and their length extends further along the aft body as the Reynolds number increases. It should be noted that the striation patterns downstream of the bow shock for each Re case are found to be consistent with those present in the corresponding z -vorticity field, as shown in Fig. 8.

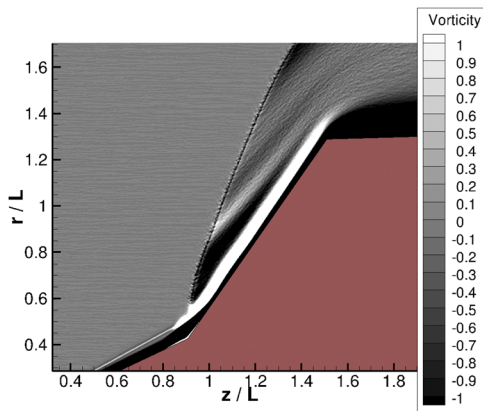


FIG. 8. Normalised vorticity in the azimuthal direction for the $Re = 93\,500\text{ m}^{-1}$ case.

B. Analysis of flow disturbances with MPT

The amplitude functions of the global modes presented in Sec. IV A clearly show the co-existence of features known from classic local linear stability theory, such as the generation of harmonic disturbances behind a shock,¹⁷ sign changes in the amplitude function of the global mode along the strong bow-shock,⁶ or spatially amplifying shear layer seen in Figs. 5–7(d) at all Reynolds numbers examined, in addition to the previously not seen feature of the repeating diagonal structure between the two sonic lines and the progression of λ -shock patterns beneath the shear layer, as seen in Figs. 7(a)–7(d) and 7(f) at the highest Reynolds number results. All these structures have been shown to be integral parts of the amplitude function of a (single) linearly decaying global mode.

In this section, the flows are further analyzed without invoking the assumption of small-perturbations but, rather, by applying MPT to the full field $\mathbf{q}(x, y, t)$ obtained from the unsteady DSMC simulation. Figure 9 shows the radial and axial components of the acoustic and the axial component of entropy fields at the lowest $Re = 93\,500\text{ m}^{-1}$ case of the momentum density term defined in Eq. (3). The spatial variation of the fields is found to be almost uniform, but the radial and axial components of the acoustic field show a sign change downstream of the bow shock. The magnitude of the thermal field is approximately a factor of 5 lower in comparison to the acoustic counterparts and shows striation patterns in the shear layer region and downstream of the bow shock that are consistent with those present in the vorticity field and the corresponding amplitude functions. It should be noted that at these conditions the contribution of both acoustic and thermal fields to the momentum density is small (i.e., $\bar{\mathbf{B}} \gg \nabla\phi_A + \nabla\phi_T$).

In order to see the effects of the Reynolds number on the spatial distribution of the acoustic and thermal fields, the Reynolds number is increased by a factor of two in comparison to the previous case. Figure 10 shows the variation of the axial and radial derivative of the scalar potential field. A comparison of Fig. 9 with Fig. 10 reveals that the spatial distribution of the acoustic, as well as the thermal field, is found to be similar in most locations; see, for example, $1.1 < z/L < 1.4$ and $1.1 < r/L < 1.3$. However, in the vicinity of the separation region and the region between A and B, shown in Figs. 10(a) or 10(b), the structure is quite different. In particular, there is a sign change in the acoustic field in this region which is at the same location where the sign change in the amplitude functions occurs, as can be seen in the bow-shock region of Fig. 6(f). A comparison of Fig. 10(d) with Fig. 9(d) suggests that the extent of the thermal component in the vicinity of the separation region increases with Re due to shearing forces along the contact surface of the separation region.

As the Reynolds number is increased further to the high $-Re$ case, the region A-B-C-D where the acoustic field changes sign grows, as shown in Figs. 11(a) and 11(b), and large acoustic and thermal potential variations are seen in the vicinity of the separation shock. Moreover, the extent of the λ -shocklet structure increases along the second cone surface, and their effect on the acoustic field becomes more prominent. Alternating signs of the radial and axial components of the acoustic field in both this region and the separation shock suggests that

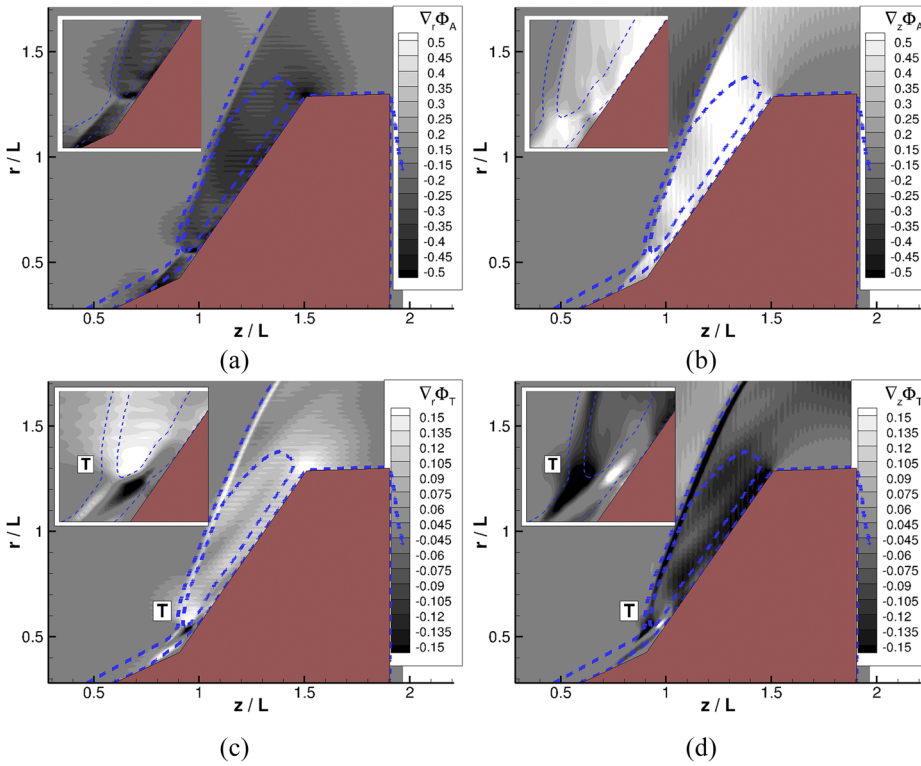


FIG. 9. Contribution of the normalized irrotational component to the momentum density at $t = 16.33$ for the $Re = 93\,500\text{ m}^{-1}$ case. Here and in Figs. 10–12, the blue lines show the shock locations and sonic line and T denotes the triple point. (a) Radial derivative of the acoustic field. (b) Axial derivative of the acoustic field. (c) Radial derivative of the thermal field. (d) Axial derivative of the thermal field.

the striations in the bow shock are an outcome of the acoustic disturbances generated at these locations. The interactions of the λ -shocklets with the shear layer create acoustic disturbances that can propagate in the upstream direction and interact with shock waves. This results in spatial changes in the shock and sonic line structures similar to those seen in the inviscid solution of Ref. 25 as well as a reflection of the acoustic waves and generation of the entropy and vorticity waves, as reported in the work of McKenzie and Westphal.¹⁶

Note that the sign change in the amplitude functions shown in the high $-Re$ results of Fig. 7(f) is consistent with the acoustic part of the momentum density changing its sign in the bow shock, as seen in Fig. 11(b). Figure 11(c) shows that the thermal component of the scalar potential is non-uniformly distributed downstream of the bow shock. Most of the variations are in fact found in the vicinity of the shear layer indicated by blue-dashed lines, i.e., in the separation zone and along the supersonic stream on the second cone surface. When the

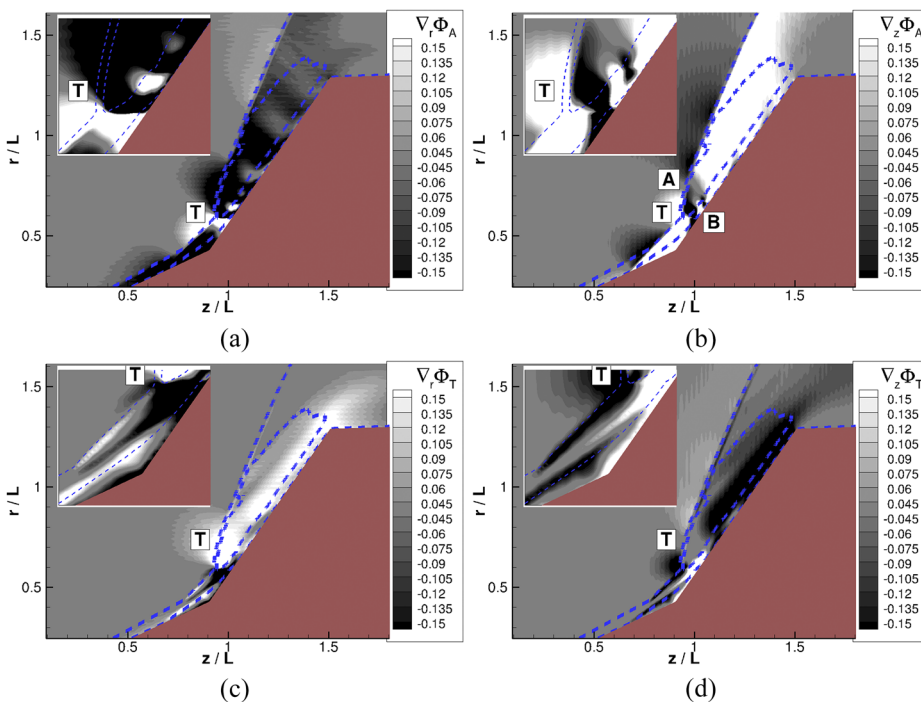


FIG. 10. Time variation of the axial derivative of the acoustic field at 24.48 for the $Re = 187\,000\text{ m}^{-1}$ case. (a) Radial derivative of the acoustic field. (b) Axial derivative of the acoustic field. (c) Radial derivative of the thermal field. (d) Axial derivative of the thermal field.

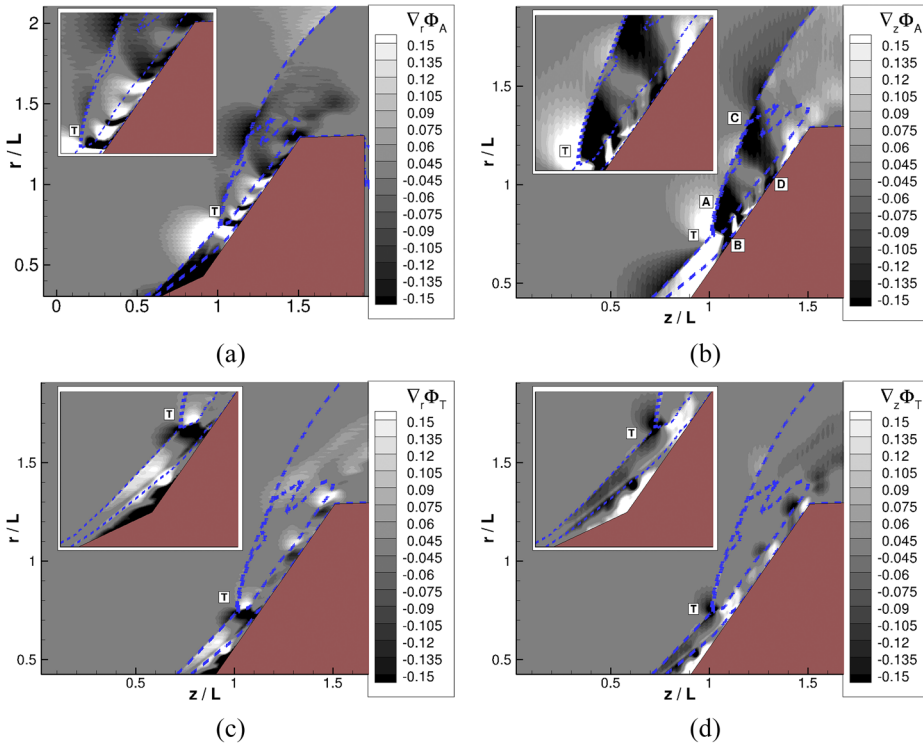


FIG. 11. Spatial distribution of the thermal and acoustic parts of the momentum density at $t = 102$ for $Re = 374\,000\text{ m}^{-1}$. (a) Radial derivative of the acoustic field. (b) Axial derivative of the acoustic field. (c) Radial derivative of the thermal field. (d) Axial derivative of the thermal field.

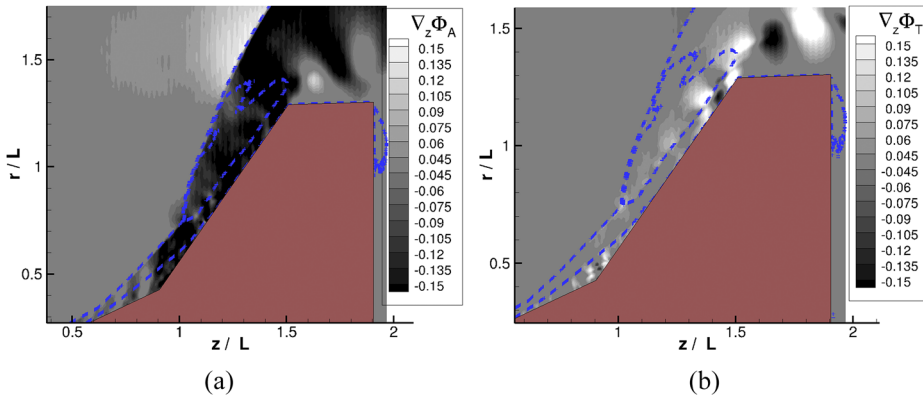


FIG. 12. Spatial distribution of the thermal and acoustic parts of the momentum density at $t = 214.3$ for $Re = 374\,000\text{ m}^{-1}$. (a) Axial derivative of the acoustic field. (b) Axial derivative of the thermal field.

flow reaches the steady state, the acoustic and thermal fields must vanish in order for Eq. (3) to hold. As time progresses and the flow develops, both acoustic and thermal fields indeed become more uniform in the vicinity of the separation shock and the A-B-C-D region, as shown in Figs. 12(a) and 12(b), respectively. This time progression results in a more stable shock structure; however, there are some fluctuations at the cone shoulder due to a Kelvin-Helmholtz instability in the shear layer.

The results of both the linear stability analysis and the MPT show that there is considerable unsteadiness in the shear-layer and bow-shock regions of the flow at the highest Reynolds number. Starting with the shear layer region shown in Fig. 13, an FFT on the DSMC macroscopic parameters was performed, yielding the most dominant frequencies at locations 1 and 2, between 45 and 70 kHz, as can be seen in Fig. 14(a). Note that for the sake of brevity, only the time variation of the translational temperatures is shown. In fact, the other macroscopic flow quantities at different locations in the shear layer exhibit the same time characteristics. Despite the

discrepancy in flow geometry, these frequencies are in the same range as the values of 22–10 kHz, obtained in the experimental

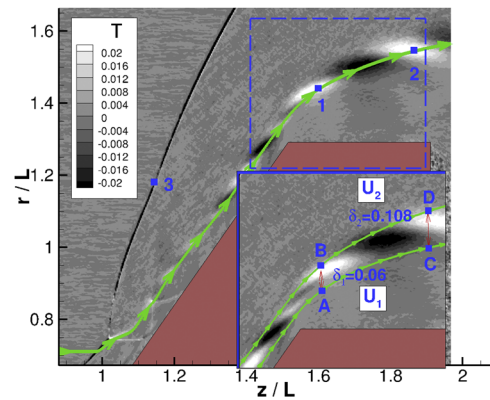


FIG. 13. Translational temperature difference between 224.5 and 214.3 superimposed probe locations in the vicinity of shear layers for the $Re = 374\,000\text{ m}^{-1}$ case. Note that the local vortical thickness is the radial distance between A-B and C-D.

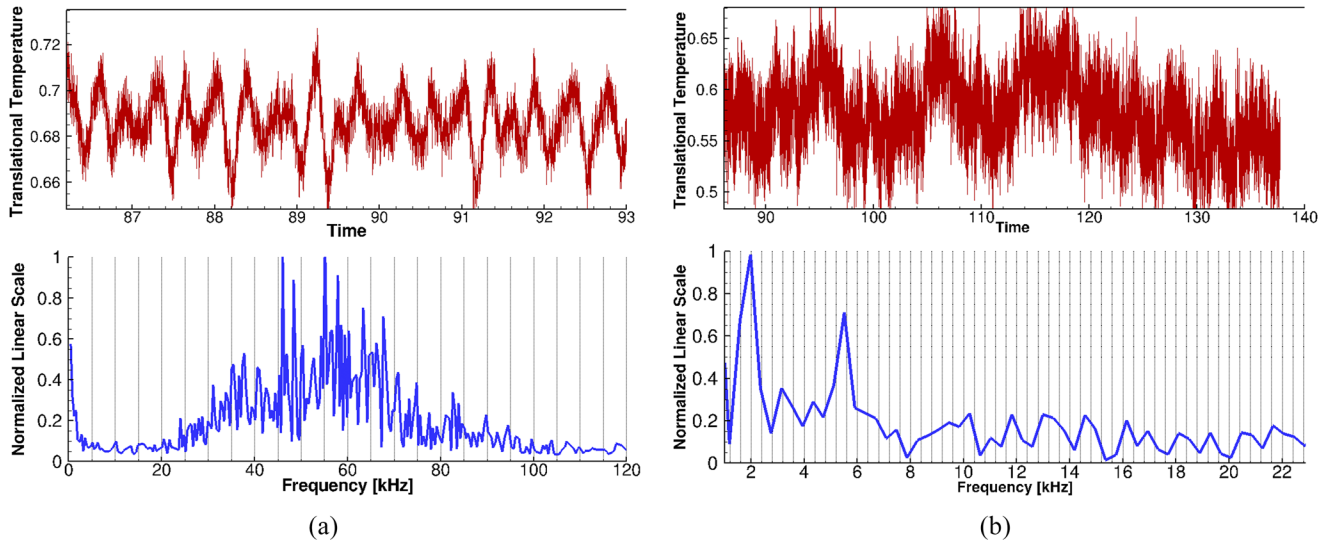


FIG. 14. Time variation of translational temperatures (red) and corresponding frequencies (blue) for $Re = 374\,000\text{ m}^{-1}$. Note that locations are shown in Fig. 13. (a) Kelvin-Helmholtz instability at location 1. (b) Low-frequency shock oscillation at location 3.

work of Martens *et al.*²⁶ for a supersonic two-stream, shear-layer flow. It should be noted that in the latter work, the pressure was a factor of 80 higher than that in the present work, the convective Mach number was 0.5, and it was found that the most dominant frequency decreased in the downstream region as the shear layer thickened. Here, the dominant frequencies essentially remain the same in the two downstream conditions, but the convective Mach number (0.32–0.185) and other macroscopic parameters changed much more rapidly between points 1 and 2. As shown in Fig. 13, organized, coherent, and large structures are observed in the shear layer, consistent with the experimental Schlieren image of Clemens and Mungal²⁷ for the convective Mach number²⁸ of 0.28. Defining the Strouhal number, $St = \frac{f\delta_w}{U_1}$, where δ_w is the length of the interaction of the local vortical thickness, U_1 is the velocity of the fast stream, and f is the dominant frequency, the Strouhal number range obtained in our analyses is $0.2 \leq St \leq 0.37$, based on $\delta_{w1} = 6\text{ mm}$, $\delta_{w2} = 11\text{ mm}$, a fast stream velocity of 1589 m s^{-1} and 1628 m s^{-1} , and a frequency of 55 kHz for locations A-B and C-D of Fig. 13, respectively. These may be compared with the St numbers obtained by Martens²⁶ who obtained a value of 0.46 for a dominant frequency of 23 kHz, $\delta_w = 12\text{ mm}$, and $U_1 = 609\text{ m s}^{-1}$ at 17 cm downstream of the trailing edge. The St values obtained in this study and by Martens²⁶ are in good agreement, and the small differences can be attributed to the fact that the flow over the cone shoulder expands in our case in contrast to the experiments where two parallel streams interact.

Regarding bow shock wave oscillations, previous studies^{29–31} focused on shock/turbulent boundary layer interactions that cause unsteady shock motions related to both upstream and downstream conditions. The interaction of upstream disturbances with shock waves results in the high shock-motion frequencies especially for the cases in which no separation occurs.⁴ On the other hand, the shock-motion frequency of separated flows is about two orders of magnitude lower than the energetic scales of the incoming boundary layer.³⁰ Wu and Martin³¹ showed that the unsteadiness of the

separation point is highly correlated with the shock motion based on the results of a direct numerical simulation for a Mach 2.9 flow over a 24° compression ramp. Characteristic low frequencies between 0.66 and 1.24 kHz were observed based on the peak value of pressure fluctuation near the separation point, as shown in Fig. 2 of Ref. 31. Assuming that the characteristic length is the size of the separation bubble⁴ and the velocity is based on the free-stream value, they obtained a Strouhal number of $0.03 \leq St \leq 0.042$, which was found to be in good agreement with the experimental work of Ref. 29 for a Mach 5 flow over the compression ramp with a deflection angle of 28° . In the present work, the dominant frequency observed in the bow and separation shock motions is about 2 kHz, as shown in Fig. 14(b), the size of the separation is 81.4 mm, and the freestream velocity is 2073 m s^{-1} , yielding $St = 0.078$, which is approximately a factor of two larger than those reported in Refs. 29 and 31. Despite the different Mach number, due to the larger deflection angle of the second cone with a value of 55° with respect to the horizontal axis, and the fact that the present work is performed in laminar conditions, the size of the separation region in the present work is found to be about three times larger than the value of 27 mm in Ref. 31; this in turn results in a larger Strouhal number. However, if the arguments presented in Ref. 30 are followed, increasing the Mach number would result in a lower value of St such that the value in the present work would be expected to be less than that reported in the work of Wu and Martin.³¹ The explanation could be that the effect of the size of the separation region dominates over the effect of the Mach number, resulting in an about two times larger Strouhal number in the present work as compared with Strouhal numbers reported in Refs. 29 and 31. Nonetheless, the Strouhal number and the dominant frequencies in the current work were found to be in relatively better agreement with those observed for the corner shock boundary layer interactions observed in Ref. 32 where experiments were carried out in order to investigate primary and corner shock boundary layer interactions at mild back pressure ratios.

V. SUMMARY AND CONCLUSIONS

Time-accurate DSMC calculations were performed to characterize the unsteadiness of hypersonic flows over an axisymmetric cone at $Ma = 16$ and a range of different Reynolds numbers. The amplitude functions calculated based on the damping rates of the least damped eigenmode showed that flow features such as the separated flow region and the bow- and the λ -shock structures are part of the same single global mode and are strongly coupled. Momentum potential theory was then used to analyze the nature of the changes in the bow shock structures and the momentum density was decoupled into thermal and acoustic contributions. For the lowest Reynolds number case, the spatial distribution of the acoustic and thermal fields downstream of the shock wave was found to be fairly uniform. On the other hand, due to the increase of pressure in the underexpanded jet region for higher Reynolds number cases, more prominent λ -shocklets appear along the second cone surface. It was observed that these structures are an outcome of the acoustic disturbances generated in the vicinity of the separation region and λ -shock patterns. For the highest Reynolds number case, the thermal component of the momentum density was found to be large in the shear layer, but the spatial distribution of both acoustic and thermal disturbances becomes more uniform especially in the SLBLI region at later times. However, the variations at the cone shoulder are attributed to a Kelvin-Helmholtz instability with the most dominant frequencies changing between 45 and 70 kHz, corresponding to Strouhal numbers varying between 0.2 and 0.37. Large-scale, organized, and coherent KH vortices are observed in the shear layer since the convective Mach number is less than 0.32. A calculated Strouhal number of 0.08 corresponding to the bow shock oscillations qualitatively agrees reasonably well with available experimental and numerical work. The existence of shock oscillations in the highest Reynolds number results suggests that unsteadiness may arise as a consequence of physical mechanisms such as (two-dimensional) Kelvin-Helmholtz instability, instability of the λ -shocklet system, and, of course, two-dimensional instability of the laminar separation bubble at the cone junction. However, the prediction that the flow ultimately settles to a laminar two-dimensional steady state precludes the flow having transitioned to turbulence. Nevertheless, as the Reynolds number increases, the relevance of a numerically predicted two-dimensional steady flow must be examined in the light of either three-dimensional linear global instability of the two-dimensional state to non-axisymmetric perturbations, or full three-dimensional direct numerical simulation. Work along the first path has commenced and its results will be reported in due course.

ACKNOWLEDGMENTS

The research of O.T. and D.L. is being supported by the Air Force Office of Scientific Research through AFOSR Grant No. FA9550-11-1-0129 with a subcontract Award No. 2010-06171-01 to UIUC. O.T. and D.L. are also grateful for the computational resource provided on ERDC Topaz, AFRL Spirit, and Thunder. The work of V.T. is sponsored by the Air Force Office of Scientific Research, Air Force Material Command,

USAF, under Grant No. FA9550-15-1-0387 *Global transient growth mechanisms in high-speed flows with application to the elliptic cone*, and Grant No. FA9550-17-1-0115 *Global Modal and Non-Modal Instability Analyses of Shock-Induced Separation Bubbles*, with V.T. as the Principal Investigator and Dr. Ivett Leyva as the Program Officer. The authors would like to thank Professor Gaitonde and Dr. Unnikrishnan for their extensive discussions on the implementation of the MPT.

- ¹S. P. Schneider, "Hypersonic laminar-turbulent transition on circular cones and scramjet forebodies," *Prog. Aerosp. Sci.* **40**, 1–50 (2004).
- ²A. Fedorov, "Transition and stability of high-speed boundary layers," *Annu. Rev. Fluid Mech.* **43**, 79–95 (2011).
- ³D. V. Gaitonde, "Progress in shock wave/boundary layer interactions," *Prog. Aerosp. Sci.* **72**, 80–99 (2015).
- ⁴*Shock Wave–Boundary-Layer Interactions*, edited by H. Babinsky and J. K. Harvey (Cambridge University Press, 2011).
- ⁵C. Windisch, B. U. Reinartz, and S. Müller, "Investigation of unsteady Edney type IV and VII shock-shock interactions," *AIAA J.* **54**, 1846–1861 (2016).
- ⁶P. W. Duck, D. G. Lasseigne, and M. Y. Hussaini, "On the interaction between the shock wave attached to a wedge and freestream disturbances," *Theor. Comput. Fluid Dyn.* **7**, 119–139 (1995).
- ⁷K. W. Cassel, A. I. Ruban, and J. D. A. Walker, "An instability in supersonic boundary-layer flow over a compression ramp," *J. Fluid Mech.* **300**, 265–285 (1995).
- ⁸N. T. Clemens and V. Narayanaswamy, "Low-frequency unsteadiness of shock wave/turbulent boundary layer interactions," *Annu. Rev. Fluid Mech.* **46**, 469–492 (2014).
- ⁹V. Narayanaswamy, L. L. Raja, and N. T. Clemens, "Control of unsteadiness of a shock wave/turbulent boundary layer interaction by using a pulsed-plasma-jet actuator," *Phys. Fluids* **24**, 076101 (2012).
- ¹⁰S. Priebe and M. P. Martin, "Low-frequency unsteadiness in shock wave-turbulent boundary layer interaction," *J. Fluid Mech.* **699**, 1–49 (2012).
- ¹¹S. Piponniau, J.-P. Dussauge, J.-F. Debieve, and P. Dupont, "A simple model for low-frequency unsteadiness in shock-induced separation," *J. Fluid Mech.* **629**, 87–108 (2009).
- ¹²O. Tumuklu, D. A. Levin, and V. Theofilis, "Investigation of unsteady, hypersonic, laminar separated flows over a double cone geometry using a kinetic approach," *Phys. Fluids* **30**, 046103 (2018).
- ¹³P. Doak, "Momentum potential theory of energy flux carried by momentum fluctuations," *J. Sound Vib.* **131**, 67–90 (1989).
- ¹⁴M. Holden, T. Wadhams, J. Harvey, and G. Candler, "Measurements in regions of low density laminar shock wave/boundary layer interaction in hypervelocity flows and comparison with Navier-Stokes predictions," AIAA Paper 2003-1131, 2003.
- ¹⁵V. Theofilis, "On steady-state flow solutions and their nonparallel global linear instability," in *8th European Turbulence Conference, June 27–30, 2000*, edited by C. Dopazo (International Center for Numerical Methods in Engineering, Barcelona, Spain, 2000), pp. 35–38.
- ¹⁶J. F. McKenzie and K. O. Westphal, "Interaction of linear waves with oblique shock waves," *Phys. Fluids* **11**, 2350–2362 (1968).
- ¹⁷L. S. G. Kovasznay, "Turbulence in supersonic flow," *J. Aeronaut. Sci.* **20**, 657–674 (1953).
- ¹⁸S. Unnikrishnan and D. V. Gaitonde, "Acoustic, hydrodynamic and thermal modes in a supersonic cold jet," *J. Fluid Mech.* **800**, 387–432 (2016).
- ¹⁹G. A. Bird, *Molecular Gas Dynamics and the Direct Simulation of Gas Flows* (Clarendon, Oxford, England, UK, 1994).
- ²⁰O. Tumuklu, D. A. Levin, and V. Theofilis, "On the temporal evolution in laminar separated boundary layer shock-interaction flows using DSMC," AIAA Paper 2017-1614, 2017.
- ²¹V. Theofilis and T. Colonius, "An algorithm for the recovery of 2- and 3-d biglobal instabilities of compressible flow over 2-d open cavities," AIAA Paper 2003-4143, 2003.
- ²²F. Gómez, S. L. Clainche, P. Paredes, M. Hermanns, and V. Theofilis, "Four decades of studying global linear instability: Progress and challenges," *AIAA J.* **50**, 2731–2743 (2012).
- ²³L. Brown, R. Boyce, N. Mudford, and S. O'Byrne, "Intrinsic three-dimensionality of laminar hypersonic shock wave/boundary layer interactions," AIAA Paper 2009-7205, 2009.
- ²⁴J. D. Crouch, A. Garbaruk, D. Magidov, and A. Travin, "Origin of transonic buffet on aerofoils," *J. Fluid Mech.* **628**, 357–369 (2009).

- ²⁵J. Olejniczak, M. J. Wright, and G. V. Candler, “Numerical study of inviscid shock interactions on double-wedge geometries,” *J. Fluid Mech.* **352**, 1–25 (1997).
- ²⁶S. Martens, K. W. Kinzie, and D. K. McLaughlin, “Measurements of Kelvin-Helmholtz instabilities in a supersonic shear layer,” *AIAA J.* **32**, 1633–1639 (1994).
- ²⁷N. T. Clemens and M. G. Mungal, “Large-scale structure and entrainment in the supersonic mixing layer,” *J. Fluid Mech.* **284**, 171–216 (1995).
- ²⁸D. Papamoschou and A. Roshko, “The compressible turbulent shear layer: An experimental study,” *J. Fluid Mech.* **197**, 453–477 (1988).
- ²⁹M. E. Erenkil and D. S. Dolling, “Unsteady wave structure near separation in a Mach 5 compression ramp interaction,” *AIAA J.* **29**, 728–735 (1991).
- ³⁰J. P. Dussauge, P. Dupont, and J. F. Debiève, “Unsteadiness in shock wave boundary layer interactions with separation,” *Aerosp. Sci. Technol.* **10**, 85–91 (2006).
- ³¹M. Wu and M. P. Martin, “Analysis of shock motion in shockwave and turbulent boundary layer interaction using direct numerical simulation data,” *J. Fluid Mech.* **594**, 71–83 (2008).
- ³²M. Funderburk and V. Narayanaswamy, “Experimental investigation of primary and corner shock boundary layer interactions at mild back pressure ratios,” *Phys. Fluids* **28**, 086102 (2016).